Engineering 7 (2021) 991–1001

Contents lists available at ScienceDirect

Engineering

journal homepage: www.elsevier.com/locate/eng

Research
Green Chemical Engineering—Review

Phosphorene-Based Heterostructured Photocatalysts

Yun Zheng [a,b], Yilin Chen [a], Bifen Gao [a], Bizhou Lin [a], Xinchen Wang [b,*]

[a] Xiamen Key Laboratory of Optoelectronic Materials and Advanced Manufacturing, College of Materials Science and Engineering, Huaqiao University, Xiamen 361021, China
[b] State Key Laboratory of Photocatalysis on Energy and Environment, College of Chemistry, Fuzhou University, Fuzhou 350116, China

ARTICLE INFO

Article history:
Received 15 April 2019
Revised 30 July 2019
Accepted 20 August 2019
Available online 4 June 2021

Keywords:
Phosphorene
Heterostructure
Photocatalysis
Water splitting
Pollutant degradation

ABSTRACT

Semiconductor photocatalysis is a potential pathway to solve the problems of global energy shortage and environmental pollution. Black phosphorus (BP) has been widely used in the field of photocatalysis owing to its features of high hole mobility, adjustable bandgap, and wide optical absorption range. Nevertheless, pristine BP still exhibits unsatisfactory photocatalytic activity due to the low separation efficiency of photoinduced charge carriers. In recent years, the construction of heterostructured photocatalysts based on BP has become a research hotspot in photocatalysis with the remarkable improvement of photoexcited charge-separation efficiency. Herein, progress on the design, synthesis, properties, and applications of BP and its corresponding heterostructured photocatalysts is summarized. Furthermore, the photocatalytic applications of BP-based heterostructured photocatalysts in water splitting, pollutant degradation, carbon dioxide reduction, nitrogen fixation, bacterial disinfection, and organic synthesis are reviewed. Opportunities and challenges for the exploration of advanced BP-based heterostructured photocatalysts are presented. This review will promote the development and applications of BP-based heterostructured photocatalysts in energy conversion and environmental remediation.

1. Introduction

Photocatalysis is a renewable and economic technology aimed at energy and environmental applications [1,2]. Research on semiconducting photocatalysis was stimulated in 1972 by the pioneering investigation of Fujishima and Honda [3] on TiO_2 electrodes for photoelectrochemical water splitting. To date, plenty of photocatalysts have been designed and developed, most of which are transition-metal-based semiconductors. Based on chemical composition, they can be classified as oxides (e.g., TiO_2) [4], sulfides (e.g., SnS_2) [5], phosphides (e.g., CoP) [6], nitrides (e.g., Ta_3N_5) [7], oxynitrides (e.g., $BaNbO_2N$) [8], and more. Since the discovery of the activity of melon-based carbon nitride (denoted as CN) polymer in photocatalytic water splitting [9], non-metal photocatalysts have started to receive more attention in photocatalysis [10]. Subsequent emergences of non-metal photocatalysts include selenium [11], sulfur [12], boron [13], doped graphene [14], and red phosphorus (RP) [15]. The development of a photocatalyst that can efficiently utilize visible and near-infrared (NIR) light and have high photoexcited charge separation/transfer efficiency is highly desirable in order to pursue the maximum utilization efficiency of solar energy [16,17].

Recently, black phosphorus (BP), also known as phosphorene, as an emerging single-element two-dimensional (2D) material, has received great attention in photocatalysis due to its fascinating features, which include a layer-dependent direct bandgap (0.3–2.1 eV), strong visible and NIR light absorption ability, high carrier mobility (~1000 $cm^2 \cdot V^{-1} \cdot s^{-1}$), in-plane structural anisotropy, low toxicity, and biocompatibility [18–20]. These properties enable BP to serve as a potential catalyst for water splitting and other photoredox reactions [21,22]. However, a pristine BP photocatalyst also suffers from shortcomings, which include the rapid recombination of photoexcited electron holes, and therefore exhibits moderate catalytic activity in many photoredox reactions [23]. Accordingly, the construction of BP-based heterostructures can suppress the recombination of photogenerated charge and carriers, thus remarkably enhancing photocatalytic activity [24].

This article provides a comprehensive review of the design, synthesis, properties, and photocatalytic applications of BP-based heterostructured photocatalysts. BP-based heterostructured photocatalysts can be classified into semiconductor/BP heterostructures, carbon materials/BP heterostructures, metal/BP heterostructures, and BP-based ternary heterostructures, based

* Corresponding author.
E-mail address: xcwang@fzu.edu.cn (X. Wang).

https://doi.org/10.1016/j.eng.2021.06.004

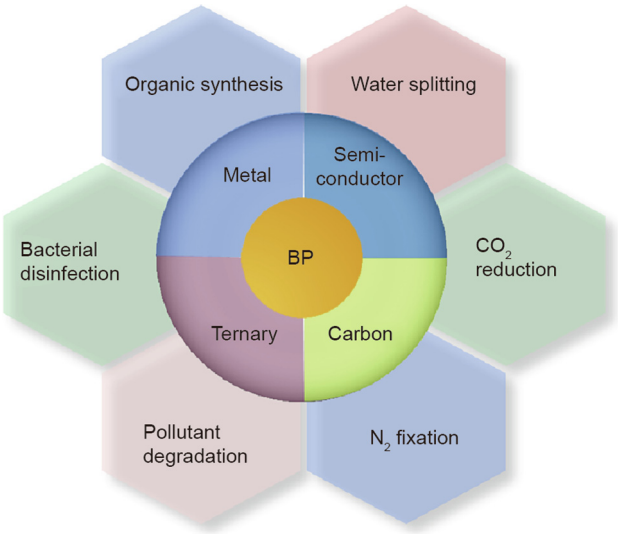

Fig. 1. Schematic illustration of the categories and photocatalytic applications of BP-based heterostructures.

on the chemical composition of the second component (Fig. 1). This article also presents the applications of BP-based photocatalysts in water splitting, pollutant degradation, bacterial disinfection, carbon dioxide (CO_2) reduction, nitrogen (N_2) fixation, and selective organic synthesis. Some perspectives and challenges in this area are also presented, which will stimulate the research interests of the chemistry, materials science, physics, and engineering communities.

2. BP-based photocatalysts for water splitting

2.1. The mechanism of BP nanosheets for water splitting

The band structure of 2D BP semiconductors has been investigated by density functional theory (DFT) calculation. BP has a bandgap of 1.79 eV under 7% tensile strain along the *a* axis and a bandgap of 1.82 eV under 5% tensile strain along the *b* axis at pH 8.0 (Fig. 2) [25]. The conduction band minimum (CBM) of BP engineered with strain is more negative than the H^+/H_2 potential, while the valence band maximum (VBM) is more positive than the O_2/H_2O potential [25]. Therefore, BP could serve as a potential photocatalyst for visible-light-driven water splitting due to the suitable bandgaps and band edge alignments [25].

2.2. Design and synthesis of BP nanosheets for water splitting

In the past decades, a great deal of research effort has been spent on the preparation of monolayer or few-layer BP (FP). The synthetic methods of 2D BP can be divided into top-down methods (e.g., liquid exfoliation, microwave exfoliation, and ball milling) and bottom-up methods (e.g., hydrothermal and solvothermal methods) [26]. Zhu et al. [27] showed that BP nanosheets prepared by a ball-milling method (BP-BM) exhibited higher photocatalytic activity in H_2 evolution than bulk BP, without using a cocatalyst (Fig. 3). The formation of BP nanosheets leads to an enlarged bandgap, improved electron-reduction ability, accelerated electron-hole separation rate, and enlarged specific surface area, resulting in enhanced photocatalytic activity in H_2 evolution [27]. In addition, BP nanosheets prepared by a solvothermal method and loaded with platinum (Pt) can generate H_2 from pure water, and possess a 24-fold higher H_2 evolution rate than CN nanosheets [28]. The partial oxidation of the surface of BP leads to the increase of both

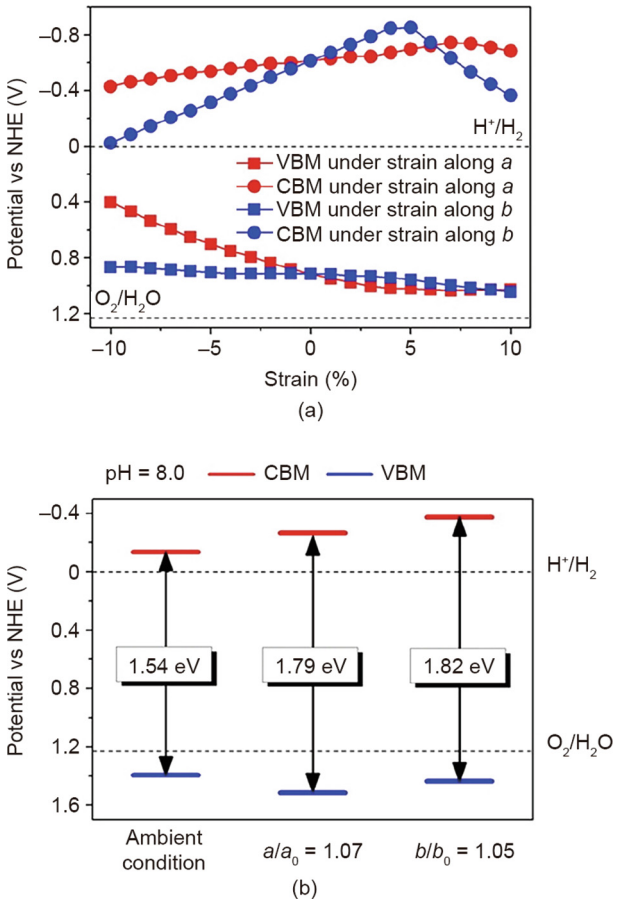

Fig. 2. (a) Formation of the conduction band minimum (CBM) and valence band maximum (VBM) of BP by introducing uniaxial strain using Heyd–Scuseria–Ernzerhof (HSE06) functional; (b) band edge alignments of BP under ambient condition or engineered with uniaxial strain. NHE: normal hydrogen electrode. Reproduced from Ref. [25] with permission of American Chemical Society, ©2014.

the photocatalytic activity and stability of BP nanosheets [28]. The synthesis of FP nanosheets with a top-down or bottom-up approach brings us a step closer to real-world applications of BP-based photocatalysts for solar energy conversion.

In addition, the hydrogen evolution rate (HER) of BP nanosheets in photocatalytic water splitting can be improved by surface modification and dye sensitization [16]. Functionalized BP with indium (III) chloride, tris(pentafluorophenyl)borane, and a benzyl group showed stability under ambient conditions and exhibited higher HER than pristine BP [16]. The HER activity of BP was also significantly improved when Eosin Y was used as the photosensitizer [16].

2.3. Recent advances of BP-based heterostructured photocatalysts in water splitting

Although pristine 2D BP has gained great attention as a potential candidate for photocatalytic water decomposition, the high charge recombination of charge carriers and the poor stability of BP nanosheets restricts their practical application. The heterostructure construction can promote the spatial separation of photoinduced electrons and holes and can endow photocatalysts with optimized photocatalytic performance [29,30]. This section discusses the development of metal/BP, semiconductor/BP, carbon materials/BP, and BP-based ternary heterostructures in photocatalytic water splitting. The photocatalytic activities of BP-based

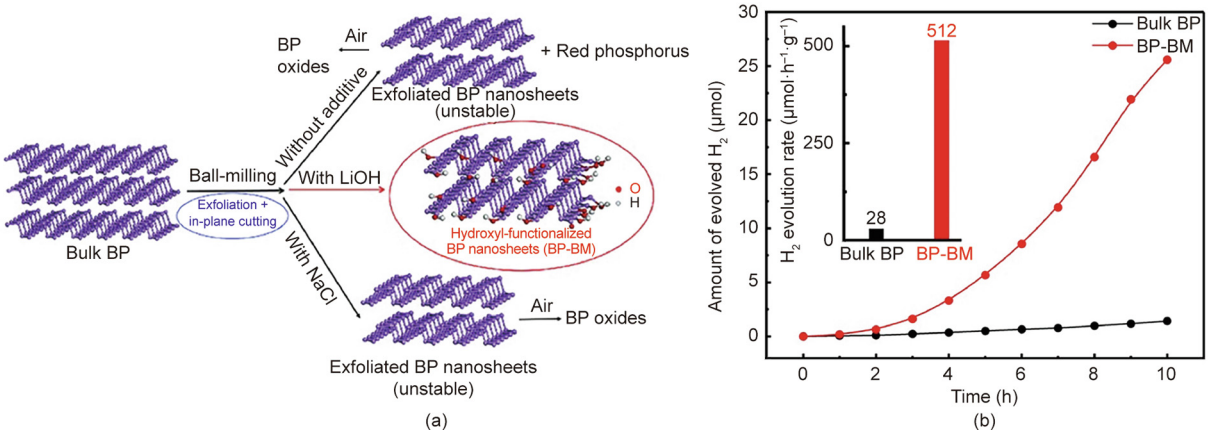

Fig. 3. (a) The synthetic process of BP-BM; (b) photocatalytic water-splitting activities of BP-BM photocatalysts under visible-light irradiation ($\lambda > 420$ nm). Reproduced from Ref. [27] with permission of Wiley-VCH Verlag GmbH & Co. KGaA, ©2017.

photocatalysts in H_2 evolution are summarized in Table 1 [23,26–29,31–53].

Construction of a metal/BP heterostructure is an important method to enhance the photocatalytic activities in hydrogen evolution. With Pt loaded as a cocatalyst, BP nanosheets prepared using the hydrothermal method exhibited superior photocatalytic H_2 evolution activity, which was attributed to the layered polycrystalline structure and stronger light absorption ability of BP [29].

In addition, BP has been coupled with various semiconductors (e.g., metal oxide, metal sulfide, metal phosphide, metal vanadate, and CN) to constitute highly efficient photocatalytic water-splitting systems [31,32]. In these hybrid systems, BP serves as a non-metal cocatalyst to raise the photocatalytic activities of the semiconductors in water decomposition, due to the following advantages: ① a large surface area and abundant active sites; ② a tuneable band gap that can be used to form a suitable band structure with other semiconductors; and ③ high mobility for shuttling photogenerated charges [33]. For example, a BP nanosheet/TiO_2 mesocrystal hybrid was utilized as a photocatalyst for H_2 evolution under visible and NIR light when depositing with Pt as a cocatalyst, because the hybrid could harvest ultraviolet (UV) to NIR light and exhibited high charge-separation efficiency [34]. Furthermore, the hybridization of FP with CdS contributed to a remarkably enhanced photocatalytic H_2 evolution rate [35]. The beneficial band structure, remarkable charge mobility, and abundant active sites of BP, as well as the intimate electronic interaction between BP and CdS, are the major reasons for the promoted photocatalytic activity of BP/CdS toward H_2 evolution (Fig. 4) [35]. Apart from that, the 2D/2D heterostructure of WS_2/BP [36] and MoS_2/BP [37] photocatalysts can effectively accelerate the separation of charge carriers, and increase the H_2 evolution rate under visible light and NIR light illumination. Moreover, an apparent quantum efficiency (AQE) of 42.55% at 430 nm for H_2 evolution and solar-to-hydrogen conversion efficiency of 5.4% was obtained when using CoP/BP nanosheets as a photocatalyst in pure water without hole scavengers and bias [38]. The efficient utilization of solar light by BP nanosheets and the high efficiency of charge-carrier separation by amorphous CoP contributed to the enhanced photocatalytic activity of CoP/BP in water splitting [39].

Metal-free heterostructured photocatalysts composed of BP and CN were designed and prepared for water splitting under visible and NIR light irradiation [40]. The strong interfacial contact and efficient charge transfer between BP and CN via the formation of N–P bonds contributed to the improved photocatalytic activity of the BP/CN hybrids for H_2 evolution (Fig. 5) [40]. Moreover, the intimate electronic coupling and accelerated charge separation and migration in the 2D/2D van der Waals heterostructure resulted in more superior photocatalytic activity and stability of the BP/CN heterostructure in H_2 evolution [41]. In addition, phosphorene quantum dots (QDs) were coupled with layered CN to form a zero-dimensional (0D)/2D heterojunction in order to facilitate free carriers' separation and improve photocatalytic activities for water splitting [42–44]. The enhanced photocatalytic activity of BP QDs/CN is ascribed to the type II band alignment, the formation of P–C bonds, and the efficient interfacial charge separation between BP QDs and CN.

To improve the photocatalytic activity of BP, the hybrid nanostructure that is formed by the combination of BP and carbon materials has attracted extensive attention. Benefiting from the efficient charge transfer between Pt/reduced graphene oxide (RGO) and excited BP nanoflakes, the BP/Pt/RGO hybrid can serve as a photocatalyst for water splitting under visible and NIR light illumination [45]. When Pt nanoparticles, BP, and RGO coexisted, the H_2 generation amounts reached about 5.13 and 1.26 μmol under > 420 and > 780 nm irradiation for 4 h, respectively [45].

Aside from the H_2 evolution half-reaction, BP-based materials have also been applied to the water oxidation half-reaction. The BP-$Ni(OH)_2$ hybrid exhibited an O_2 production rate of 15.7 μmol per gram catalyst per hour or 224.3 μmol per gram BP per hour under simulated sunlight illumination [54]. Furthermore, overall water splitting was realized over a Z-scheme heterostructure artificial photosynthetic system composed of 2D BP/$BiVO_4$. In this photosystem, the O_2 generation reaction was driven by the photogenerated holes in the valence band (VB) of $BiVO_4$, while the H_2 evolution reaction was initiated by the photogenerated electrons in the conduction band (CB) of BP [47]. These discoveries demonstrate the promising prospect of semiconductor/BP heterostructured photocatalysts in water splitting.

Extensive effort has been focused on the design of BP-based binary nanocomposites for photocatalytic water splitting. To further improve the physicochemical properties and photocatalytic activities, BP-based ternary composites have been developed. The construction of a ternary heterostructure by combining wide-bandgap semiconductors, narrow-bandgap semiconductors, and metal takes full advantage of the respective superiorities of each component, hence providing an effective approach to realize better photocatalytic performance. BP–Au/$La_2Ti_2O_7$ can be utilized as a broadband solar-response photocatalyst for H_2 production, because plasmonic gold (Au) and BP can harvest broadband light, and electrons can efficiently migrate from BP and Au to $La_2Ti_2O_7$ (Fig. 6) [48]. Furthermore, BP QDs–Au–CdS [49], BP QDs–CdS–$La_2Ti_2O_7$ [50] and CdS/BP–MoS_2 [51] heterostructures can efficiently photocatalytically generate H_2 for a wide solar spectrum, and show higher H_2 production rates than those of binary hybrids. Moreover,

Table 1
Summary of the photocatalytic activities of BP-based photocatalysts in H_2 evolution.

Photocatalyst	Heterojunction type	Cocatalyst	Sacrificial agent	Light source	Mass of catalyst	HER	AQE and wavelength	Stability	Ref.
BP-BM	—	—	Na_2S/Na_2SO_3	Xe, 300 W, > 420 nm	5 mg	2.6 μmol·h^{-1}	0.47% (420 nm)	10 h	[27]
BP nanosheets	—	—	TEOA	Xe, 300 W, > 420 nm	0.2 mg	0.01 μmol·h^{-1}	—	40 h	[23]
BP nanoparticles	—	—	TEOA	Xe, 300 W, > 420 nm	0.8 mg	0.04 μmol·h^{-1}	—	40 h	[23]
BP nanosheets	—	—	TEOA	Xe, 300 W, > 420 nm	5 mg	17.9 μmol·h^{-1}	3.9% (420 nm)	36 h	[26]
BP nanosheets	—	Pt	Methanol	Xe, 300 W, > 420 nm	50 mg	6.9 μmol·h^{-1}	—	30 h	[29]
BP nanosheets	—	—	—	Xe, 300 W, > 420 nm	25 mg	0.37 μmol·h^{-1}	—	12 h + 4 months	[28]
BP nanosheets	—	Pt	—	Xe, 300 W, > 420 nm	25 mg	11.2 μmol·h^{-1}	3.8% (420 nm)	20 h	[28]
BP/TiO_2	Z-scheme	Pt	TEOA	Xe, 300 W	25 mg	51.7 μmol·h^{-1}	18.23% (365 nm)	18 h	[33]
BP/TiO_2 mesocrystal	Type II	Pt	Methanol	Asahi Spectra Hal-320, 200 mW·cm^{-2}, > 420 nm	2 mg	1.9 μmol·h^{-1}	7.1% (420 nm)	12 h	[34]
BP/TiO_2 mesocrystal	Type II	Pt	Methanol	Asahi Spectra Hal-320, 200 mW·cm^{-2}, > 780 nm	2 mg	0.41 μmol·h^{-1}	1.2% (780 nm)	—	[34]
BP/CdS	Type II	—	Lactic acid	Xe, 300 W, > 420 nm	20 mg	223.8 μmol·h^{-1}	34.7% (420 nm)	20 h	[35]
$Zn_xCd_{1-x}S/BP$	Type II	—	Lactic acid	Xe, 300 W, > 420 nm	20 mg	186.5 μmol·h^{-1}	21.5% (420 nm)	20 h	[31]
$BP_{15.2}/Zn_{0.5}Cd_{0.5}S$	—	—	Na_2S/Na_2SO_3	Xe, 300 W, > 420 nm	10 mg	1371.7 μmol·h^{-1}	36.3 % (420 nm)	27 h	[32]
$BP_{15.2}/Zn_{0.5}Cd_{0.5}S$	—	—	Na_2S/Na_2SO_3	Xe, 300 W, > 510 nm	10 mg	269.6 μmol·h^{-1}	—	—	[32]
BP/WS_2	—	—	EDTA	Xe, 320 W, ≥ 780 nm	0.22 mg	0.8 μmol·h^{-1}	2.06% (780 nm, 1.1 mg catalyst)	12 h + 1 month	[36]
BP/WS_2	—	—	EDTA	Portable infrared laser, 2 W, 808 nm	0.22 mg	0.5 μmol·h^{-1}	—	3 h	[36]
BP/MoS_2	—	—	Na_2S/Na_2SO_3	Xe, 300 W, > 420 nm	10 mg	12.86 μmol·h^{-1}	1.2% (420 nm)	12 h	[37]
CoP/BP	—	—	—	Xe, 300 W, > 420 nm	40 mg	15 μmol·h^{-1}	42.55% (430 nm)	40 h	[38]
CoP/BP	—	—	Oxalic acid	Xe, 300 W, ≥ 420 nm	2 mg	1.4 μmol·h^{-1}	—	16 h + 2 days	[39]
$BP/BiVO_4$	Z-scheme	—	EDTA	Xe, 320 W, > 420 nm	5 mg	2.5 μmol·h^{-1}	0.89% (420 nm)	9 h	[47]
MBWO/BP	Z-scheme	Pt	TEOA	Xe, 300 W, Vis light, > 420 nm	20 mg	84.1 μmol·h^{-1}	—	25 h	[46]
BP/CN	Type I	—	Methanol	Xe, 320 W, > 420 nm	1.5 mg	0.6 μmol·h^{-1}	3.2% (420 nm, 10 mg catalyst)	21 h + 2 weeks	[40]
BP/CN	Type I	—	Methanol	Xe, 320 W, > 780 nm	1.5 mg	0.2 μmol·h^{-1}	1.1% (780 nm)	—	[40]
BP/CN	Type I	—	Lactic acid	Xe, 300 W, ≥ 400 nm	20 mg	11.4 μmol·h^{-1}	1.2% (420 nm)	14 h	[41]
BP/CN	Type I	—	Isopropanol	LED, 440–445 nm	2 mg	1.57 μmol·h^{-1}	—	18 h	[53]
BP QDs/CN	Type II	—	Methanol	Xe, 200 W, simulated sunlight	100 mg	190 μmol·h^{-1}	—	25 h	[42]
BP QDs/CN	Type II	—	Methanol	LED, 405 nm	100 mg	133 μmol·h^{-1}	—	5 h	[42]
BP QDs/CN	Type II	—	Methanol	LED, 420 nm	100 mg	90 μmol·h^{-1}	—	5 h	[42]
BP QDs/CN	Type II	—	Methanol	LED, 550 nm	100 mg	10.4 μmol·h^{-1}	—	5 h	[42]
BP QDs/CN	Type II	Pt	Methanol	Xe, 300 W, ≥ 420 nm	39.6 mg	10.7 μmol·h^{-1}	—	32 h	[43]
BP QDs/reticulated CN	Type II	Pt	TEOA	Xe, 300 W, > 420 nm	10 mg	138.3 μmol·h^{-1}	16.5% (420 nm)	36 h	[44]
BP/Pt/RGO	—	—	EDTA	Xe, 320 W, > 420 nm	0.375 mg	1.3 μmol·h^{-1}	8.7% (420 nm, 1.88 mg catalyst)	20 h	[45]
BP/Pt/RGO	—	—	EDTA	Xe, 320 W, > 780 nm	0.375 mg	0.3 μmol·h^{-1}	1.5% (780 nm, 1.88 mg catalyst)	4 h	[45]
BP/Pt/RGO	—	—	EDTA	Portable infrared laser, 2 W, 808 nm	0.375 mg	0.2 μmol·h^{-1}	—	4 h	[45]
$BP–Au/La_2Ti_2O_7$	—	—	Methanol	Xe, 320 W, > 420 nm	1.5 mg	1.1 μmol·h^{-1}	—	12 h	[48]
$BP–Au/La_2Ti_2O_7$	—	—	Methanol	Xe, 320 W, > 780 nm	1.5 mg	0.5 μmol·h^{-1}	—	12 h	[48]
BP QDs–Au–CdS	—	—	Na_2S/Na_2SO_3	Xe, 300 mW·cm^{-2}, > 420 nm	20 mg	172 μmol·h^{-1}	2.3% (900 nm)	18 h + 3 weeks	[49]
BP QDs–CdS–$La_2Ti_2O_7$	—	—	Na_2S/Na_2SO_3	Xe, 300 mW·cm^{-2}, UV–Vis–NIR	20 mg	19.2 μmol·h^{-1}	—	15 h	[50]
BP QDs–CdS–$La_2Ti_2O_7$	—	—	Na_2S/Na_2SO_3	Xe, 300 mW·cm^{-2}, Vis–NIR, > 420 nm	20 mg	16 μmol·h^{-1}	2.2% (420 nm)	—	[50]
BP QDs–CdS–$La_2Ti_2O_7$	—	—	Na_2S/Na_2SO_3	Xe, 300 mW·cm^{-2}, NIR, > 700 nm	20 mg	5.2 μmol·h^{-1}	0.5% (700 nm)	—	[50]
$CdS/BP–MoS_2$	—	—	Lactic acid	Xe, 150 W, 100 W·m^{-2}, a solar simulator, AM 1.5G filter	1 mg	183.2 μmol·h^{-1}	63.1% (425 nm)	60 h	[51]
Ni_2P at BP/CN	—	—	TEOA	Xe, 300 W, ≥ 420 nm	20 mg	17.2 μmol·h^{-1}	2.8% (420 nm)	20 h	[52]

AQE: apparent quantum efficiency; TEOA: triethanolamine; EDTA: ethylene diamine tetraacetic acid; MBWO: monolayered Bi_2WO_6; QD: quantum dot; LED: light-emitting diode; RGO: reduced graphene oxide; UV: ultraviolet; Vis: visible.

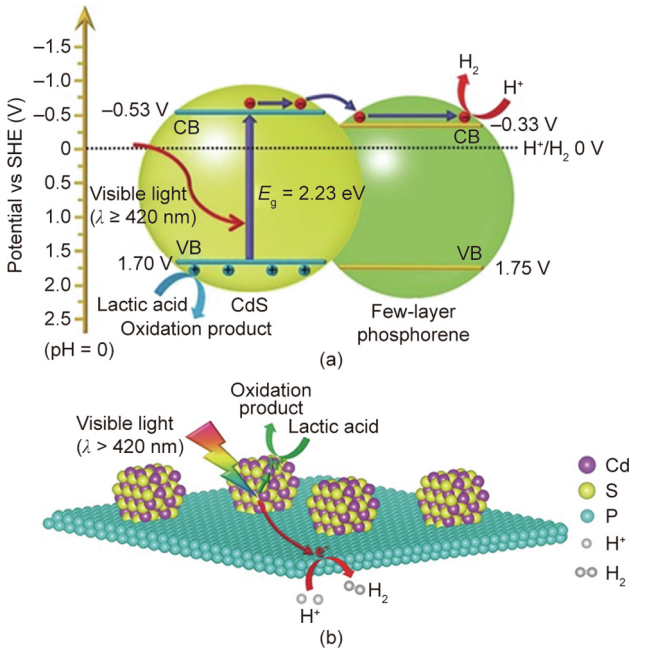

Fig. 4. Schematic illustration of the photocatalytic mechanism of the CdS/BP hybrid for water splitting. SHE: standard hydrogen electrode; CB: conduction band; VB: valence band; E_g: band gap energy. Reproduced from Ref. [35] with permission of Wiley-VCH Verlag GmbH & Co. KGaA, ©2017.

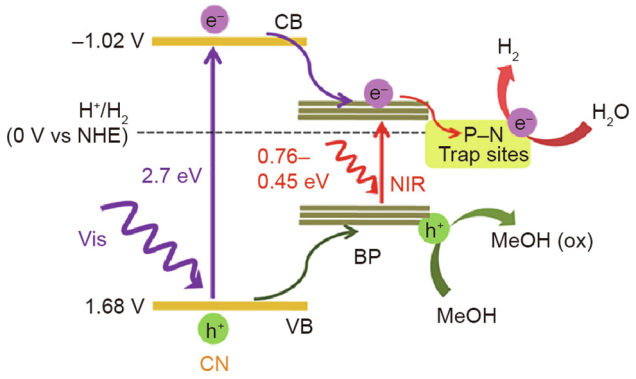

Fig. 5. Schematic diagram for the photocatalytic water-splitting mechanism over BP/CN. Ox: oxidation. Reproduced from Ref. [40] with permission of American Chemical Society, ©2017.

2D BP-supported Ni_2P can act as an earth-abundant cocatalyst to couple with a 2D porous CN nanosheet to further enhance visible-light photocatalytic H_2 production activity [52]. These findings demonstrate the superiority of BP-based heterostructured photocatalysts in water splitting.

3. BP-based photocatalysts for pollutant treatment and bacterial disinfection

BP-based photocatalysts have stimulated continuous research interest due to their promising photocatalytic application in pollutant treatment. With the advantages of their unique electronic structure and physicochemical properties, BP and its hybrids have been used for the photocatalytic degradation of various pollutants, such as rhodamine B (RhB), reactive black 5 (RB 5), methyl orange (MO), methylene blue (MB), 2-chlorophenol (2-CP), bisphenol A (BPA), 1,3-diphenylisobenzofuran (DPBF), dibutyl phthalate (DBP), Cr(VI), and NO. This section discusses the application of BP nanosheets, BP QDs, and BP-based heterostructured photocatalysts in pollutant treatment.

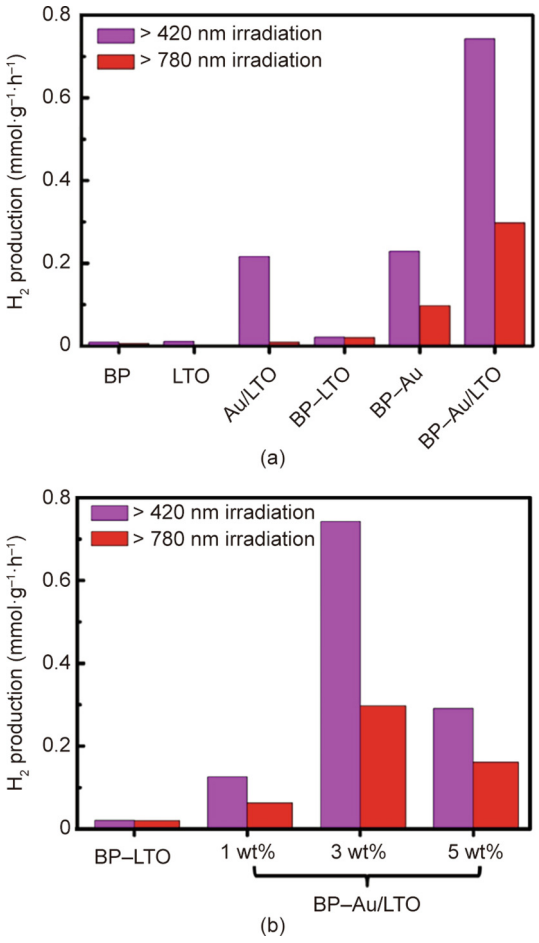

Fig. 6. (a) Photocatalytic H_2 evolution over BP–Au/$La_2Ti_2O_7$ (LTO) under Vis–NIR (>420 nm) and NIR (>780 nm) light irradiation; (b) effect of the Au ratio on photocatalytic H_2 evolution rate for BP–Au/$La_2Ti_2O_7$. Reproduced from Ref. [48] with permission of Wiley-VCH Verlag GmbH & Co. KGaA, ©2017.

3.1. BP nanosheets and BP QDs for pollutants treatment

The molecular oxygen activation and pollutant degradation ability of 2D BP nanosheets has aroused great research interest. Ultrathin 2D BP nanosheets were prepared by Wang et al. [55] via a sonication-mediated liquid exfoliation method in degassed water (Fig. 7). The BP nanosheets served as a photosensitizer for singlet oxygen ($^1O_2$) production with a high quantum yield of about 0.91 [55]. Furthermore, ultrathin BP nanosheets also present an exotic, excitation-energy-related, optical-switching effect in the production of reactive oxygen species (ROS) [56]. The primary ROS products are hydroxyl radicals (·OH) and $^1O_2$ under UV and visible-light irradiation, respectively. BP nanosheets exhibited excellent activity in the photocatalytic degradation of MO under different illumination conditions [56]. In another case, $^1O_2$ and $O_2^{\cdot-}$ were generated by energy/charge transfer from the excited P* to the ground state of O_2 when 2D BP nanosheets, oxygen, water, and light coexisted [57]. The photodegradation efficiency of DBP for 2D BP nanosheets was greatly improved via the $^1O_2$ oxidation reaction, whereas the effects of $O_2^{\cdot-}$ with lower oxidative reactivity were negligible. These findings indicate a promising technique for the removal of water-soluble organic pollutants by 2D BP-based photocatalysts [57].

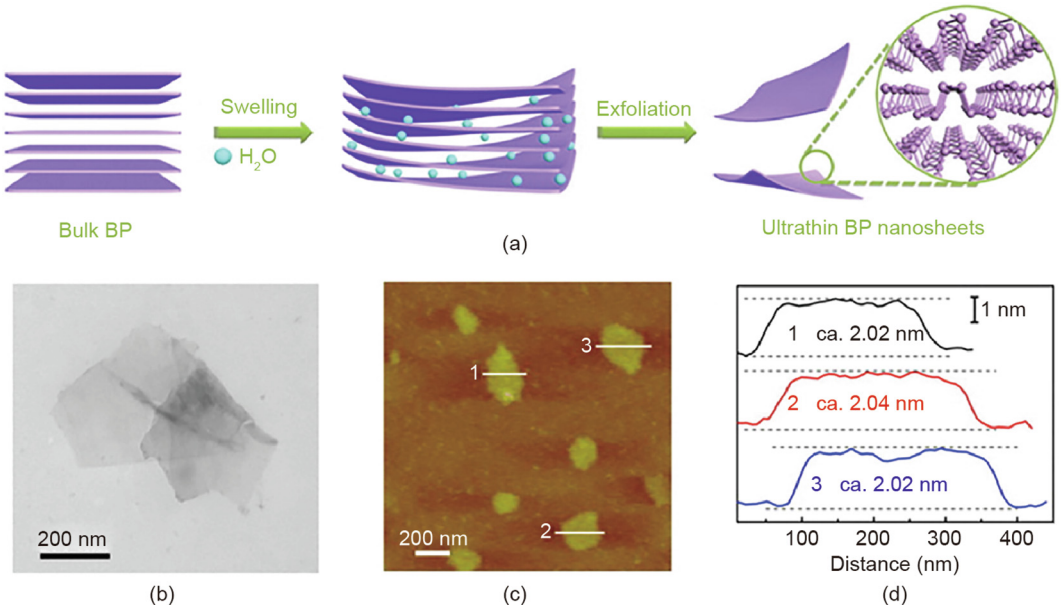

Fig. 7. (a) Synthetic process of ultrathin BP nanosheets; (b) transmission electron microscope (TEM) image; (c) atomic force microscope image; (d) corresponding height image of ultrathin BP nanosheets. Reproduced from Ref. [55] with permission of American Chemical Society, ©2015.

In addition, bandgap-tunable BP QDs were prepared by Yuan et al. [58] via a liquid exfoliation approach in a mixed solvent of oleic acid and *N*-methyl pyrrolidone. The as-prepared BP QDs with a bandgap of 2.82 eV showed high photocatalytic activity for RhB degradation [58]. The major ROS products, ·OH and $O_2^{\cdot-}$, account for the superior photocatalytic activities of BP QDs for RhB degradation. Furthermore, a heterostructure of BP QDs and attapulgite (BP QDs/ATP) demonstrated higher photocatalytic activity toward the decomposition of BPA due to the sensitization of BP QDs and the facilitation of charge separation [59]. The development of BP-based photocatalysts will open up new opportunities for environmental remediation [59].

3.2. BP-based heterostructured photocatalysts for pollutant treatment and bacterial disinfection

Diverse categories of BP-based heterostructured photocatalysts have been developed for pollutant degradation, including semiconductor/BP, carbon materials/BP, metal/BP, and BP-based ternary composites [60]. This section discusses the progress that has been made on the application of these heterostructures for pollutant degradation. The photocatalytic activities of BP-based photocatalysts in pollutant degradation are summarized in Table 2 [46,53,55–59,61–68,70–75].

The loading of metal nanoparticles on BP to construct a metal/BP heterostructure is a key method for enhancing photocatalytic activity. Plasmonic Ag/BP nanohybrids synthesized via a chemical reduction approach were applied to photocatalytic pollutant degradation (Fig. 8) [61]. When decreasing the layer thickness of BP from multi-layers to few-layers, or increasing the size of the silver (Ag) nanoparticles, Ag/BP plasmonic nanohybrids exhibited higher photocatalytic activity than pristine BP nanosheets in RhB degradation. This research opens a new path for the application of plasmonic metal/BP nanohybrids in photocatalytic pollutant degradation [61].

Various semiconductors, such as TiO_2, CeO_2, MoS_2, RP, and CN, have been coupled with BP to form heterostructures with improved photocatalytic activity for pollutant degradation [62]. Lee et al. [63] were the first to apply FP–titanium dioxide (BP@TiO_2) hybrids to pollutant degradation and bacterial disinfection. In comparison with BP, TiO_2, and P25, BP@TiO_2 hybrid showed a higher rate constant in the decomposition of anionic (RB 5) and cationic (RhB) dyes, and exhibited higher photocatalytic activity in bacterial disinfection with visible-light illumination [63]. The heterojunction between FP and TiO_2 promotes photoinduced charge-carrier separation with the injection of electrons from the CB of TiO_2 to FP, while the holes trapped from the VB in the FP and/or TiO_2 will have longer lifetimes [63]. In addition, CeO_2/BP hybrids with oxygen vacancies were prepared by a hydrothermal and deposition approach [64]. The photocatalytic degradation rate of BPA for the CeO_2/BP composite reached 82.3% within 180 min, which was higher than that of the individual counterparts [64]. The Z-scheme heterostructure was responsible for the optimized photocatalytic degradation activity, because of the accelerated charge-carrier separation rate and the high redox potential of the photogenerated charge carriers [64]. Furthermore, a 0D/2D nanohybrid of BP QDs/MoS_2 was formed by anchoring BP QDs onto MoS_2 nanosheets via a grinding and sonicating approach [65]. The enhanced photocatalytic activity of the BP QDs/MoS_2 in MO decomposition originates from its type II band alignment, improved light-harvesting ability, and accelerated spatial charge separation [65]. A hybrid nanocomposite of a zeolitic imidazolate framework (ZIF-8) and BP (ZIF-8/BP) was formed by functionalizing BP with polyvinylpyrrolidone [66]. Since 2D BP functions as an effective electron acceptor and promotes the charge separation and transfer in ZIF-8, the ZIF-8/BP composites exhibited higher photocatalytic reactivity toward the degradation of MB [66]. In addition to the photodecomposition of pollutants in the liquid phase, BP-based heterostructured photocatalysts have been designed and applied to the removal of NO gas. A Z-scheme 2D/2D heterojunction of monolayered Bi_2WO_6/BP (MBWO/BP) showed improved photocatalytic performance in NO removal to purify air [46]. $O_2^{\cdot-}$, ·OH, NO_2, and NO_3^- species were detected in the reaction (Fig. 9) [46].

In addition to the construction of metal-containing semiconductor and BP hybrids, the design of metal-free heterostructured photocatalysts has stimulated great research interest. An RP/BP heterostructure, which was synthesized via a high-energy ball-milling technique, showed remarkably higher photocatalytic activity in the degradation of RhB than those of pristine RP and CdS [67]. Aside from the ball-milling method, RP/BP heterostructure prepared using a microwave-assisted liquid-phase synthetic method

Table 2
Summary of the photocatalytic activities of BP-based photocatalysts in pollutant degradation.

Photocatalyst	Heterojunction type	Pollutant	Light source	Time	Removal rate	Degradation rate	Stability	Ref.
BP	—	MO	Xe, ≥ 600 nm	20 min	90%	0.115 min^{-1}	—	[55]
BP	—	DPBF	Xe, ≥ 600 nm	15 min	50%	0.046 min^{-1}	—	[55]
BP	—	MO	Xe, ≥ 420 nm	25 min	90%	0.092 min^{-1}	10 h	[56]
BP	—	DBP	Xe	360 min	45%	0.0025 min^{-1}	6 h	[57]
BP QDs	—	RhB	Xe, 300 W, > 420 nm	180 min	—	0.0135 min^{-1}	9 h	[58]
Ag/BP	—	RhB	Xe, 300 W, > 420 nm	—	—	0.057 min^{-1}	—	[61]
BP QDs/attapulgite	Type II	BPA	Xe, 300 W	180 min	90%	0.013 min^{-1}	3 h	[59]
BP/TiO_2	—	RB 5	UV, 4 W, < 365 nm	70 min	—	0.071 min^{-1}	17.5 h	[63]
BP/TiO_2	—	RB 5	Xe, 150 W, > 420 nm	70 min	—	0.040 min^{-1}	17.5 h	[63]
BP/TiO_2	—	RhB	UV, 4 W, < 365 nm	70 min	—	0.077 min^{-1}	17.5 h	[63]
BP/TiO_2	—	RhB	Xe, 150 W, > 420 nm	70 min	—	0.034 min^{-1}	17.5 h	[63]
TiO_2 at BP	—	RhB	Xe, 300 W, UV–Vis light	120 min	98%	—	6 h	[62]
BP/CeO_2	Z-scheme	BPA	Xe, 300 W	180 min	82.3%	—	3 h	[64]
BP QDs/MoS_2	Type II	MO	Xe, 300 W, > 420 nm	40 min	—	0.052 min^{-1}	8 h	[65]
BP QDs/MoS_2	Type II	MO	Xe, 300 W, > 780 nm	60 min	—	0.03 min^{-1}	2.2 h	[65]
ZIF-8/BP	—	MB	Hg, 500 W	60 min	90%	0.045 min^{-1}	1 h	[66]
MBWO/BP	—	NO	Xe, 300 W, Vis light	30 min	67%	—	3 h	[46]
RP/BP	—	RhB	Xe, 300 W, > 420 nm	30 min	—	0.069 min^{-1}	7 h	[67]
RP/BP	—	MB	Xe, 300 W, > 400 nm	180 min	91%	—	3 h	[68]
BP/CN	Type I	RhB	Xe, 300 W, > 420 nm	30 min	—	0.288 min^{-1}	6 h	[70]
BP/CN	Type I	RhB	LED, 440–445 nm	30 min	—	0.10 min^{-1}	1.5 h	[53]
BP/C_{60}	—	2-CP	Xe, 300 W, > 420 nm	50 min	—	0.112 min^{-1}	5 h + 1 week	[71]
Graphene–BP	—	2-CP	Xe, 300 W, > 420 nm	180 min	87.08%	0.011 min^{-1}	15 days	[72]
BP–Ag/TiO_2	—	MB	Xe, 300 W, > 420 nm	85 min	100%	0.029 min^{-1}	4.25 h	[73]
BP–Ag/TiO_2	—	MB	Xe, 300 W, > 780 nm	85 min	25%	0.003 min^{-1}	4.25 h	[73]
Ag–BP NS/GO	—	MB	Xe, 300 W, > 420 nm	90 min	—	0.0313 min^{-1}	9 h + 1 week	[74]
BP/CN/MOFs	—	NO	Xe, 300 W, Vis light	30 min	74%	—	2.5 h	[75]

ZIF: zeolitic imidazolate framework.

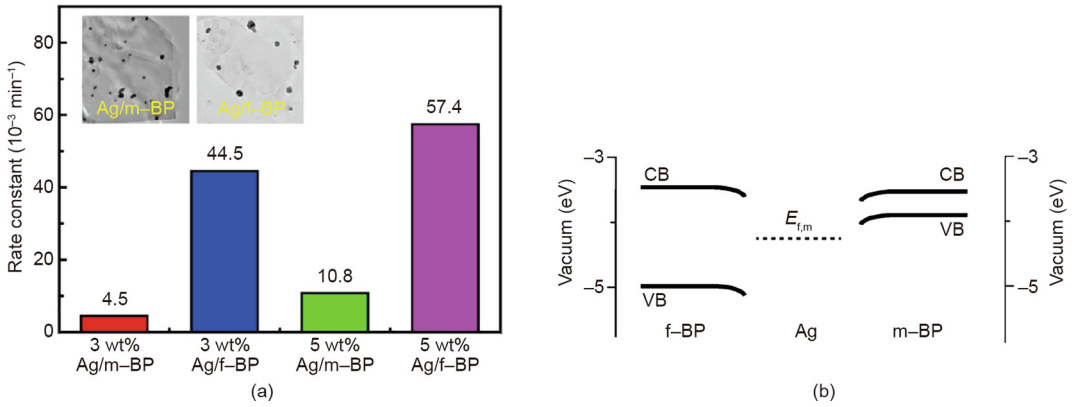

Fig. 8. (a) Photocatalytic activities of Ag/multi-layered BP (m-BP) and Ag/few-layered BP (f-BP) hybrids for RhB degradation (insets show the TEM images of Ag/m-BP and Ag/f-BP); (b) energy bands of f-BP, Ag, and m-BP. $E_{f,m}$: Fermi energy level. Reproduced from Ref. [61] with permission of American Chemical Society, ©2016.

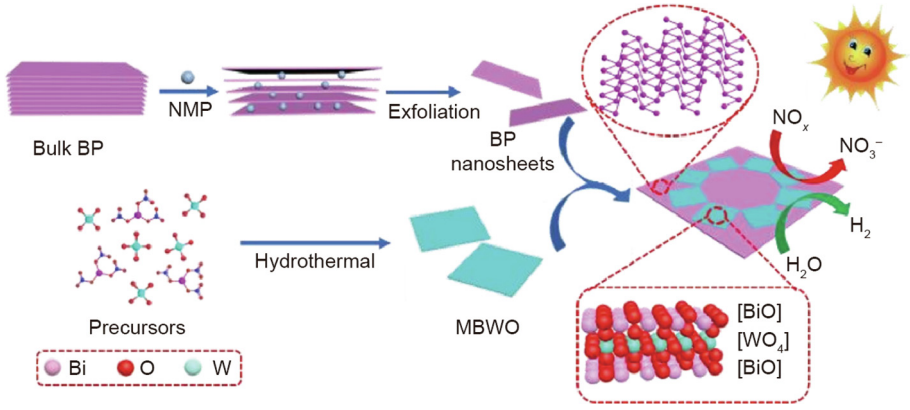

Fig. 9. Synthetic process of the MBWO/BP heterojunction. NMP: *N*-methyl-pyrrolidone. Reproduced from Ref. [46] with permission of Wiley-VCH Verlag GmbH & Co. KGaA, ©2019.

showed superior photocatalytic ability in MB decomposition with visible-light irradiation [68].

Furthermore, a metal-free heterostructure composed of BP/CN was designed and applied to the photocatalytic removal of RhB and Cr(VI) [69]. BP/CN hybrids were synthesized using a one-step liquid exfoliation strategy in *N*-methyl-pyrrolidone (NMP) [70]. The BP/CN hybrids showed enhanced photocatalytic activity in the degradation of RhB, which was mainly ascribed to the stronger visible-light harvesting capability, accelerated charge-separation rate, and enhanced ability in ROS generation (Fig. 10) [70]. To lower the preparation cost, a BP/CN heterostructured photocatalyst was synthesized from urea and RP via a ball-milling technique [53]. The BP/CN heterostructure also exhibited superior photocatalytic activity in the degradation of RhB, which was attributed to accelerated charge separation and migration, and the formation of P–N bonds [53].

Carbon materials/BP heterostructures with enhanced stability and photocatalytic activity have shown great potential in pollutant degradation. The edge-selective functionalization of BP nanosheets by the covalent bonding of C_{60} molecules via covalent P–C bonds was accomplished via a ball-milling method [71]. The participation of C_{60} results in photoinduced electron transfer from BP to C_{60}, and hinders the recombination of charge carriers, thus greatly increasing the stability and photocatalytic activity of the BP–C_{60} hybrid in RhB degradation [71]. In another case, graphene–BP hybrids were synthesized using a chemical vapor transport approach under mild growth conditions [72]. The graphene–BP hybrid displayed higher photocatalytic performance in the removal of 2-CP than BP under visible-light irradiation, owing to the promoted transfer of photoexcited charge carriers [72]. This breakthrough of hybridizing BP nanosheets with carbon materials opens up a new path toward environmental manipulation.

BP-based ternary composites have been designed and developed to further promote their photocatalytic activity in pollutant degradation and air purification. Benefiting from a better harvest of solar light and improved charge-separation efficiency, a Ag/TiO_2 nanohybrid sensitized by BP nanosheets (BP–Ag/TiO_2) showed outstanding photocatalytic performance in MB degradation under visible and NIR light illumination [73]. Ag–BP/graphene oxide also exhibited promoted photocatalytic activity in the decomposition of MB, which was attributed to the broad-spectrum response of the BP nanosheets and the effective trapping of electrons by the Ag nanoparticles [74]. In addition, a ternary heterojunction composed of BP, porous CN, and metal–organic framework (BP/CN/MOF) was utilized as a macroscopic membrane material for the photocatalytic removal of NO [75]. The nanocomposite showed higher photocatalytic performance than CN-related heterojunctions in NO removal under visible-light illumination [75]. These ternary nanocomposites will become effective photofunctional materials in environmental remediation.

The studies described above hold great promise for the preparation of highly efficient BP-based heterostructured photocatalysts toward environmental remediation.

4. BP-based photocatalysts for N_2 fixation, CO_2 reduction, and selective organic photosynthesis

In addition to applications in water splitting and pollutant degradation, BP-based heterostructures have been used in N_2 fixation, CO_2 reduction, and selective organic photosynthesis. The

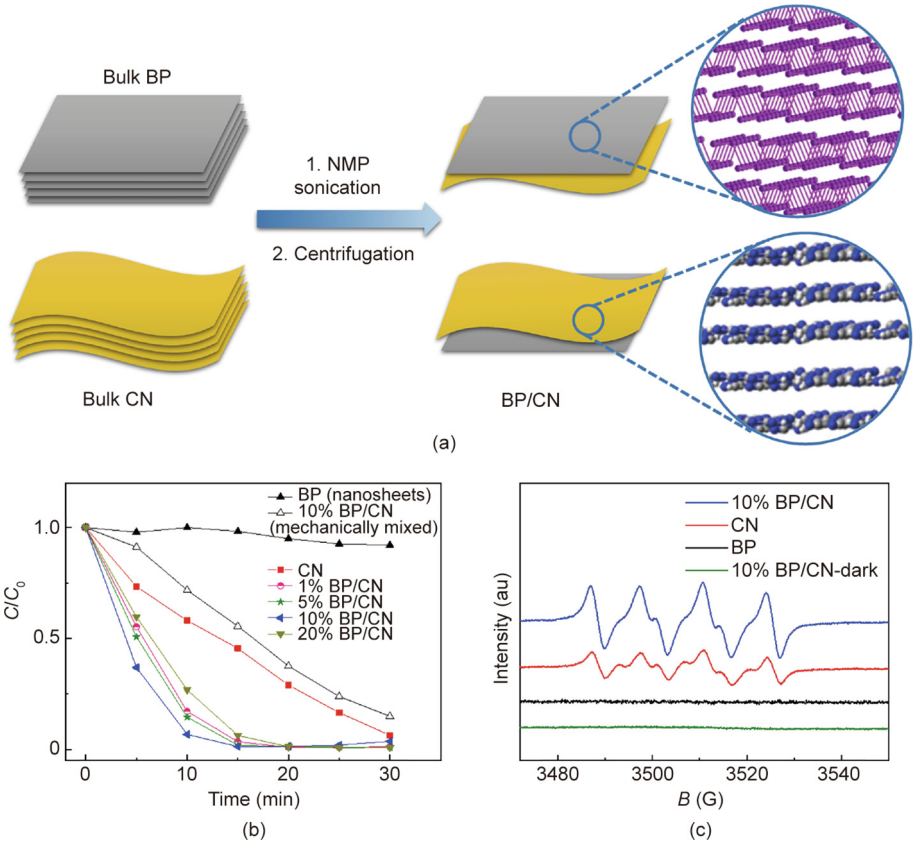

Fig. 10. (a) Schematic illustration of the synthetic process of the BP/CN heterostructure; (b) photocatalytic activities of BP/CN hybrids in RhB degradation (C_0 is the initial concentration of RhB, and C is the concentration of RhB after photocatalytic reaction); (c) electron paramagnetic resonance spectra of 10% BP/CN hybrid for the detection of $O_2^{\cdot-}$ radicals (B is magnetic field, 1 G = 10^{-4} T). Reproduced from Ref. [70] with permission of Wiley-VCH Verlag GmbH & Co. KGaA, ©2018.

composite of BP and CN nanosheets (BPCNS) exhibits high activity in photocatalytic N_2 fixation (Fig. 11) [69]. The photocatalytic N_2 fixation rate of 0.05BPCNS (0.05 means the mass ratio of BP to CN nanosheets is 0.05) is 347.5 μmol·L^{-1}·h^{-1}, which is more than eight times higher than that of CNS (40.5 μmol·L^{-1}·h^{-1}) [69]. The electrons in 0.05BPCNS can be excited more easily due to the change of the π-conjugated CN system and the formation of C–P bonds [69]. Recombination of photogenerated charge carriers is suppressed due to the efficient transfer of photogenerated electrons via the formation of C–P bonds [69]. Some of the lone pairs on phosphorus atoms are occupied, owing to the formation of C–P bonds in 0.05BPCNS, and the oxidation of BP is inhibited by reducing the number of oxygen reactive sites. In addition, BP QDs-modified CN composites can act as a candidate to initiate the photocatalytic reaction of CO_2 reduction [76]. In comparison with pristine CN (2.65 μmol·h^{-1}·g^{-1}), BP/CN composites exhibited enhanced carrier-separation efficiency and higher activities for photocatalytic CO_2 reduction to CO (6.54 μmol·h^{-1}·g^{-1}) [76].

2D BP has also been used for a solar-to-chemical energy conversion reaction, in which triethylamine (TEA) was oxidized to TEA^+, and chloro(triphenylphosphine)gold(I) (Au^ITPP) was converted to Au^IBP and reduced to Au nanoparticles [77]. Furthermore, a Pt/BP heterostructure with strong Pt–P interactions and good stability has been demonstrated to show superior performance in the hydrogenation of styrene and benzaldehyde, as well as the oxidation of benzyl alcohol under simulated solar light irradiation (Fig. 12) [78].

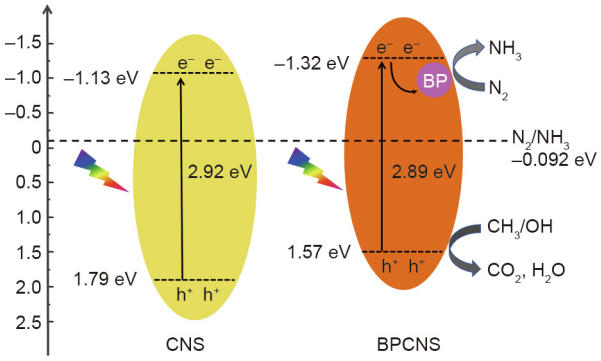

Fig. 11. The mechanism of photocatalytic nitrogen fixation over 0.05BPCNS catalyst. CNS: carbon nitride nanosheets. Reproduced from Ref. [69] with permission of Elsevier B.V., ©2018.

5. Conclusions

This review presents an overview of the synthesis, modification, and photocatalytic applications of BP-based photocatalysts. Various BP-based heterostructured photocatalysts have been designed and prepared, including metal oxide/BP, metal sulfide/BP, metal phosphide/BP, metal vanadate/BP, metal tungstate/BP, MOFs/BP, RP/BP, CN/BP, metal/BP, carbon materials/BP, and BP-based ternary composites. These BP-based heterostructured photocatalysts are promising candidates toward water splitting, pollutant degradation, disinfection, CO_2 reduction, N_2 fixation, and organic synthesis.

Despite essential advances in the development of BP-based photocatalysts, the performance of BP-based photocatalysts cannot yet satisfy the demands of practical applications. Future efforts are highly desired in the following aspects. First, the exploration of effective methods to optimize the photocatalytic properties of BP-based materials is still required. Rationally tuning the bandgap configuration and surface properties of BP is required for the design of highly efficient photocatalysts. Second, more comprehensive investigation of the reaction mechanism via theoretical calculations and *in situ* characterization techniques is necessary to clarify the thermodynamics and kinetics of the catalytic process as well as the structure–activity relationship of photocatalysts [19,20]. Third, the exploitation of suitable approaches to enhance the long-time stability of BP-based materials in photocatalytic systems is highly necessary. The degradation of BP arises from the reaction between O_2 and the lone pair electrons perpendicular to the BP surfaces, which may induce the generation of PO_x species [79]. In general, the stability of BP can be enhanced by the formation of a heterostructure. Strategies including passivation, the covalent surface modification of BP, and encapsulating BP with protective layers could also be developed and utilized to prevent the oxidation of BP from the air [80]. Finally, an environmental risk assessment of these nanostructured photocatalysts should be adequately conducted before practical application. The toxicity of intermediate products should be evaluated, since some pollutants cannot be mineralized during the photocatalytic degradation process [81]. The real commercial and industrial applications of BP-based catalysts via the photocatalytic route require more extensive investigation, and we expect their possible realization in the future, with continued efforts in this direction.

Acknowledgements

This work was financially supported by the National Natural Science Foundation of China (21902051, 21861130353, U1905214, 21961142019, 22032002, 21761132002, and

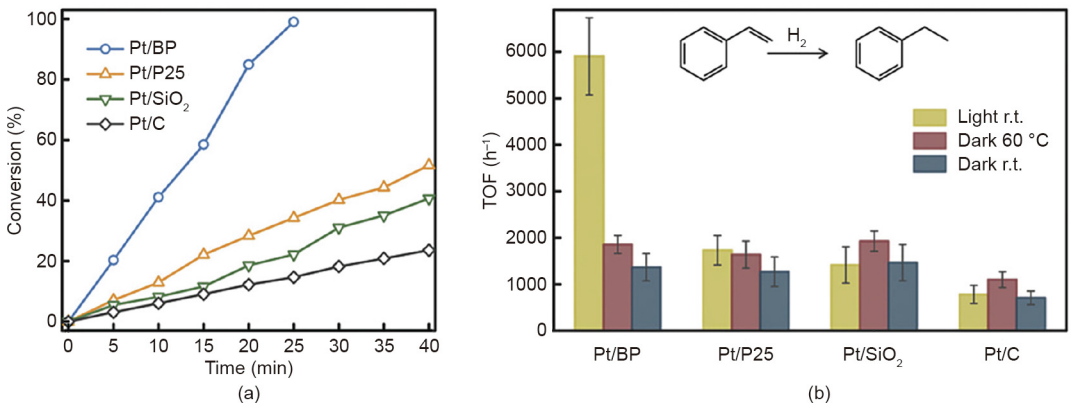

Fig. 12. (a) Conversion rates of styrene to ethylbenzene under simulated solar light illumination for Pt/BP catalysts; (b) turnover frequency (TOF) in the hydrogenation of styrene for Pt/BP. R.t.: room temperature, 28 °C. Reproduced from Ref. [78] with permission of Wiley-VCH Verlag GmbH & Co. KGaA, ©2018.

21425309), the Fundamental Research Funds for the Central Universities (ZQN-807), the Natural Science Foundation of Fujian Province (2019J05090 and 2017J01014), the Graphene Powder and Composite Research Center of Fujian Province (2017H2001), the Scientific Research Funds of Huaqiao University (20171XD033), the Open Project Program of the State Key Laboratory of Photocatalysis on Energy and Environment of Fuzhou University (SKLPEE-KF201803), the National Key Technologies R&D Program of China (2018YFA0209301), the National Basic Research Program of China (2013CB632405), the Chang Jiang Scholars Program of China (T2016147), and the 111 Project (D16008).

Compliance with ethics guidelines

Yun Zheng, Yilin Chen, Bifen Gao, Bizhou Lin, and Xinchen Wang declare that they have no conflict of interest or financial conflicts to disclose.

References

[1] Shao B, Liu X, Liu Z, Zeng G, Liang Q, Liang C, et al. A novel double Z-scheme photocatalyst $Ag_3PO_4/Bi_2S_3/Bi_2O_3$ with enhanced visible-light photocatalytic performance for antibiotic degradation. Chem Eng J 2019;368:730–45.
[2] Shao B, Liu X, Liu Z, Zeng G, Zhang W, Liang Q, et al. Synthesis and characterization of 2D/0D g-C_3N_4/CdS-nitrogen doped hollow carbon spheres (NHCs) composites with enhanced visible light photodegradation activity for antibiotic. Chem Eng J 2019;374:479–93.
[3] Fujishima A, Honda K. Electrochemical photolysis of water at a semiconductor electrode. Nature 1972;238(5358):37–8.
[4] Yu S, Yun HJ, Kim YH, Yi J. Carbon-doped TiO_2 nanoparticles wrapped with nanographene as a high performance photocatalyst for phenol degradation under visible light irradiation. Appl Catal B 2014;144:893–9.
[5] Jiao X, Li X, Jin X, Sun Y, Xu J, Liang L, et al. Partially oxidized SnS_2 atomic layers achieving efficient visible-light-driven CO_2 reduction. J Am Chem Soc 2017;139(49):18044–51.
[6] Tian J, Cheng N, Liu Q, Xing W, Sun X. Cobalt phosphide nanowires: efficient nanostructures for fluorescence sensing of biomolecules and photocatalytic evolution of dihydrogen from water under visible light. Angew Chem Int Ed Engl 2015;54(18):5493–7.
[7] Su Z, Wang L, Grigorescu S, Lee K, Schmuki P. Hydrothermal growth of highly oriented single crystalline Ta_2O_5 nanorod arrays and their conversion to Ta_3N_5 for efficient solar driven water splitting. Chem Commun 2014;50(98):15561–4.
[8] Hisatomi T, Katayama C, Moriya Y, Minegishi T, Katayama M, Nishiyama H, et al. Photocatalytic oxygen evolution using $BaNbO_2N$ modified with cobalt oxide under photoexcitation up to 740 nm. Energy Environ Sci 2013;6(12):3595–9.
[9] Wang X, Maeda K, Thomas A, Takanabe K, Xin G, Carlsson JM, et al. A metal-free polymeric photocatalyst for hydrogen production from water under visible light. Nat Mater 2009;8(1):76–80.
[10] Shao B, Liu Z, Zeng G, Wu Z, Liu Y, Cheng M, et al. Nitrogen-doped hollow mesoporous carbon spheres modified g-C_3N_4/Bi_2O_3 direct dual semiconductor photocatalytic system with enhanced antibiotics degradation under visible light. ACS Sustain Chem Eng 2018;6(12):16424–36.
[11] Chiou YD, Hsu YJ. Room-temperature synthesis of single-crystalline Se nanorods with remarkable photocatalytic properties. Appl Catal B 2011;105(1–2):211–9.
[12] Liu G, Niu P, Yin L, Cheng HM. α-Sulfur crystals as a visible-light-active photocatalyst. J Am Chem Soc 2012;134(22):9070–3.
[13] Liu G, Yin LC, Niu P, Jiao W, Cheng HM. Visible-light-responsive β-rhombohedral boron photocatalysts. Angew Chem Int Ed Engl 2013;52(24):6242–5.
[14] Xing M, Fang W, Yang X, Tian B, Zhang J. Highly-dispersed boron-doped graphene nanoribbons with enhanced conductibility and photocatalysis. Chem Commun 2014;50(50):6637–40.
[15] Hu Z, Yuan L, Liu Z, Shen Z, Yu JC. An elemental phosphorus photocatalyst with a record high hydrogen evolution efficiency. Angew Chem Int Ed Engl 2016;55(33):9580–5.
[16] Vishnoi P, Gupta U, Pandey R, Rao CNR. Stable functionalized phosphorenes with photocatalytic HER activity. J Mater Chem A 2019;7(12):6631–7.
[17] Zheng Y, Chen Y, Gao B, Chen J, Du Z, Lin B. Polymeric carbon nitride hybridized by $CuInS_2$ quantum dots for photocatalytic hydrogen evolution. Mater Lett 2019;254:81–4.
[18] Li L, Yu Y, Ye GJ, Ge Q, Ou X, Wu H, et al. Black phosphorus field-effect transistors. Nat Nanotechnol 2014;9(5):372–7.
[19] Huang YC, Chen X, Wang C, Peng L, Qian Q, Wang SF. Layer-dependent electronic properties of phosphorene-like materials and phosphorene-based van der Waals heterostructures. Nanoscale 2017;9(25):8616–22.
[20] Wang C, Peng L, Qian Q, Du J, Wang S, Huang Y. Tuning the carrier confinement in GeS/phosphorene van der Waals heterostructures. Small 2018;14(10):201703536.
[21] Rahman MZ, Kwong CW, Davey K, Qiao SZ. 2D phosphorene as a water splitting photocatalyst: fundamentals to applications. Energy Environ Sci 2016;9(3):709–28. Erratum in: Energy Environ Sci 2016;9(4):1513–4.
[22] Feng R, Lei W, Liu G, Liu M. Visible- and NIR-light responsive black-phosphorus-based nanostructures in solar fuel production and environmental remediation. Adv Mater 2018;30(49):e1804770.
[23] Muduli SK, Varrla E, Xu Y, Kulkarni SA, Katre A, Chakraborty S, et al. Evolution of hydrogen by few-layered black phosphorus under visible illumination. J Mater Chem A 2017;5(47):24874–9.
[24] Li B, Lai C, Zeng G, Huang D, Qin L, Zhang M, et al. Black phosphorus, a rising star 2D nanomaterial in the post-graphene era: synthesis, properties, modifications, and photocatalysis applications. Small 2019;15(8):e1804565.
[25] Sa B, Li YL, Qi J, Ahuja R, Sun Z. Strain engineering for phosphorene: the potential application as a photocatalyst. J Phys Chem C 2014;118(46):26560–8.
[26] Rahman MZ, Batmunkh M, Bat-Erdene M, Shapter JG, Mullins CB. p-Type BP nanosheet photocatalyst with AQE of 3.9% in the absence of a noble metal cocatalyst: investigation and elucidation of photophysical properties. J Mater Chem A 2018;6(38):18403–8.
[27] Zhu X, Zhang T, Sun Z, Chen H, Guan J, Chen X, et al. Black phosphorus revisited: a missing metal-free elemental photocatalyst for visible light hydrogen evolution. Adv Mater 2017;29(17):201605776.
[28] Tian B, Tian B, Smith B, Scott MC, Lei Q, Hua R, et al. Facile bottom-up synthesis of partially oxidized black phosphorus nanosheets as metal-free photocatalyst for hydrogen evolution. Proc Natl Acad Sci USA 2018;115(17):4345–50.
[29] Zhao G, Wang T, Shao Y, Wu Y, Huang B, Hao X. A novel mild phase-transition to prepare black phosphorus nanosheets with excellent energy applications. Small 2017;13(7):201602243.
[30] Liang Q, Liu X, Zeng G, Liu Z, Tang L, Shao B, et al. Surfactant-assisted synthesis of photocatalysts: mechanism, synthesis, recent advances and environmental application. Chem Eng J 2019;372:429–51.
[31] Ran J, Wang X, Zhu B, Qiao SZ. Strongly interactive 0D/2D hetero-structure of a $Zn_xCd_{1-x}S$ nano-particle decorated phosphorene nano-sheet for enhanced visible-light photocatalytic H_2 production. Chem Commun 2017;53(71):9882–5.
[32] Zhao H, Liu H, Sun R, Chen Y, Li X. A $Zn_{0.5}Cd_{0.5}S$ photocatalyst modified by 2D black phosphorus for efficient hydrogen evolution from water. ChemCatChem 2018;10(19):4395–405.
[33] Wu J, Huang S, Jin Z, Chen J, Hu L, Long Y, et al. Black phosphorus: an efficient co-catalyst for charge separation and enhanced photocatalytic hydrogen evolution. J Mater Sci 2018;53(24):16557–66.
[34] Elbanna O, Zhu M, Fujitsuka M, Majima T. Black phosphorus sensitized TiO_2 mesocrystal photocatalyst for hydrogen evolution with visible and near-infrared light irradiation. ACS Catal 2019;9(4):3618–26.
[35] Ran J, Zhu B, Qiao SZ. Phosphorene co-catalyst advancing highly efficient visible-light photocatalytic hydrogen production. Angew Chem Int Ed Engl 2017;56(35):10373–7.
[36] Zhu M, Zhai C, Fujitsuka M, Majima T. Noble metal-free near-infrared-driven photocatalyst for hydrogen production based on 2D hybrid of black phosphorus/WS_2. Appl Catal B 2018;221:645–51.
[37] Yuan YJ, Wang P, Li Z, Wu Y, Bai W, Su Y, et al. The role of bandgap and interface in enhancing photocatalytic H_2 generation activity of 2D–2D black phosphorus/MoS_2 photocatalyst. Appl Catal B 2019;242:1–8.
[38] Tian B, Tian B, Smith B, Scott MC, Hua R, Lei Q, et al. Supported black phosphorus nanosheets as hydrogen-evolving photocatalyst achieving 5.4% energy conversion efficiency at 353 K. Nat Commun 2018;9(1):1397.
[39] Liang Q, Shi F, Xiao X, Wu X, Huang K, Feng S. *In situ* growth of CoP nanoparticles anchored on black phosphorus nanosheets for enhanced photocatalytic hydrogen production. ChemCatChem 2018;10(10):2179–83.
[40] Zhu M, Kim S, Mao L, Fujitsuka M, Zhang J, Wang X, et al. Metal-free photocatalyst for H_2 evolution in visible to near-infrared region: black phosphorus/graphitic carbon nitride. J Am Chem Soc 2017;139(37):13234–42.
[41] Ran J, Guo W, Wang H, Zhu B, Yu J, Qiao SZ. Metal-free 2D/2D phosphorene/g-C_3N_4 van der Waals heterojunction for highly enhanced visible-light photocatalytic H_2 production. Adv Mater 2018;30(25):1800128.
[42] Kong LQ, Ji YJ, Dang ZZ, Yan JQ, Li P, Li YY, et al. g-C_3N_4 loading black phosphorus quantum dot for efficient and stable photocatalytic H_2 generation under visible light. Adv Funct Mater 2018;28(22):1800668.
[43] Lei W, Mi Y, Feng R, Liu P, Hu S, Yu J, et al. Hybrid 0D–2D black phosphorus quantum dots-graphitic carbon nitride nanosheets for efficient hydrogen evolution. Nano Energy 2018;50:552–61.
[44] Song T, Zeng G, Zhang P, Wang T, Ali A, Huang S, et al. 3D reticulated carbon nitride materials high uniformly capture 0D black phosphorus as /0D composites for stable and efficient photocatalytic hydrogen evolution. J Mater Chem A 2019;7(2):503–12.
[45] Zhu M, Osakada Y, Kim S, Fujitsuka M, Majima T. Black phosphorus: a promising two dimensional visible and near-infrared-activated photocatalyst for hydrogen evolution. Appl Catal B 2017;217:285–92.
[46] Hu J, Chen D, Mo Z, Li N, Xu Q, Li H, et al. Z-scheme 2D/2D heterojunction of black phosphorus/monolayer Bi_2WO_6 nanosheets with enhanced photocatalytic activities. Angew Chem Int Ed Engl 2019;58(7):2073–7.
[47] Zhu M, Sun Z, Fujitsuka M, Majima T. Z-scheme photocatalytic water splitting on a 2D heterostructure of black phosphorus/bismuth vanadate using visible light. Angew Chem Int Ed Engl 2018;57(8):2160–4.
[48] Zhu M, Cai X, Fujitsuka M, Zhang J, Majima T. Au/$La_2Ti_2O_7$ nanostructures sensitized with black phosphorus for plasmon-enhanced photocatalytic

hydrogen production in visible and near-infrared light. Angew Chem Int Ed 2017;56(8):2064–8.
[49] Cai X, Mao L, Yang S, Han K, Zhang J. Ultrafast charge separation for full solar spectrum-activated photocatalytic H_2 generation in a black phosphorus–Au–CdS heterostructure. ACS Energy Lett 2018;3(4):932–9.
[50] Mao L, Cai X, Yang S, Han K, Zhang J. Black phosphorus–CdS–$La_2Ti_2O_7$ ternary composite: effective noble metal-free photocatalyst for full solar spectrum activated H_2 production. Appl Catal B 2019;242:441–8.
[51] Reddy DA, Kim EH, Gopannagari M, Kim Y, Kumar DP, Kim TK. Few layered black phosphorus/MoS_2 nanohybrid: a promising co-catalyst for solar driven hydrogen evolution. Appl Catal B 2019;241:491–8.
[52] Boppella R, Yang W, Tan J, Kwon HC, Park J, Moon J. Black phosphorus supported Ni_2P co-catalyst on graphitic carbon nitride enabling simultaneous boosting charge separation and surface reaction. Appl Catal B 2019;242:422–30.
[53] Wen M, Wang J, Tong R, Liu D, Huang H, Yu Y, et al. A low-cost metal-free photocatalyst based on black phosphorus. Adv Sci 2019;6(1):1801321.
[54] Yan J, Ji Y, Kong L, Li Y, Navlani-García M, Liu S, et al. Black phosphorus-based compound with few layers for photocatalytic water oxidation. ChemCatChem 2018;10(16):3424–8.
[55] Wang H, Yang X, Shao W, Chen S, Xie J, Zhang X, et al. Ultrathin black phosphorus nanosheets for efficient singlet oxygen generation. J Am Chem Soc 2015;137(35):11376–82.
[56] Wang H, Jiang S, Shao W, Zhang X, Chen S, Sun X, et al. Optically switchable photocatalysis in ultrathin black phosphorus nanosheets. J Am Chem Soc 2018;140(9):3474–80.
[57] Pan S, He J, Wang C, Zuo Y. Exfoliation of two-dimensional phosphorene sheets with enhanced photocatalytic activity under simulated sunlight. Mater Lett 2018;212:311–4.
[58] Yuan YJ, Yang S, Wang P, Yang Y, Li Z, Chen D, et al. Bandgap-tunable black phosphorus quantum dots: visible-light-active photocatalysts. Chem Commun 2018;54(8):960–3.
[59] Li X, Li F, Lu X, Zuo S, Zhuang Z, Yao C. Black phosphorus quantum dots/attapulgite nanocomposite with enhanced photocatalytic performance. Funct Mater Lett 2017;10(6):1750078.
[60] Yan J, Verma P, Kuwahara Y, Mori K, Yamashita H. Recent progress on black phosphorus-based materials for photocatalytic water splitting. Small Methods 2018;2(12):1800212.
[61] Lei W, Zhang T, Liu P, Rodriguez JA, Liu G, Liu M. Bandgap- and local field-dependent photoactivity of Ag/black phosphorus nanohybrids. ACS Catal 2016;6(12):8009–20.
[62] Liu Y, Zhou M, Zhang W, Chen K, Mei A, Zhang Y, et al. Enhanced photocatalytic properties of TiO_2 nanosheets@2D layered black phosphorus composite with high stability under hydro-oxygen environment. Nanoscale 2019;11(12):5674–83.
[63] Lee HU, Lee SC, Won J, Son BC, Choi S, Kim Y, et al. Stable semiconductor black phosphorus (BP)@titanium dioxide (TiO_2) hybrid photocatalysts. Sci Rep 2015;5(1):8691.
[64] He C, Qian H, Li X, Yan X, Zuo S, Qian J, et al. Visible-light-driven CeO_2/black phosphorus heterostructure with enhanced photocatalytic performance. J Mater Sci Mater Electron 2019;30(1):593–9.
[65] Feng R, Lei W, Sui X, Liu X, Qi X, Tang K, et al. Anchoring black phosphorus quantum dots on molybdenum disulfide nanosheets: a 0D/2D nanohybrid with enhanced visible- and NIR-light photoactivity. Appl Catal B 2018;238:444–53.
[66] Wang L, Xu Q, Xu J, Weng J. Synthesis of hybrid nanocomposites of ZIF-8 with two-dimensional black phosphorus for photocatalysis. RSC Adv 2016;6(73):69033–9.
[67] Shen Z, Sun S, Wang W, Liu J, Liu Z, Yu JC. A black–red phosphorus heterostructure for efficient visible-light-driven photocatalysis. J Mater Chem A 2015;3(7):3285–8.
[68] He D, Zhang Z, Qu J, Yuan X, Guan J. Facile one-step synthesis of black phosphorus via microwave irradiation with excellent photocatalytic activity. Part Part Syst Charact 2018;35(11):1800306.
[69] Qiu P, Xu C, Zhou N, Chen H, Jiang F. Metal-free black phosphorus nanosheets-decorated graphitic carbon nitride nanosheets with C–P bonds for excellent photocatalytic nitrogen fixation. Appl Catal B 2018;221:27–35.
[70] Zheng Y, Yu Z, Ou H, Asiri AM, Chen Y, Wang X. Black phosphorus and polymeric carbon nitride heterostructure for photoinduced molecular oxygen activation. Adv Funct Mater 2018;28(10):1705407.
[71] Zhu X, Zhang T, Jiang D, Duan H, Sun Z, Zhang M, et al. Stabilizing black phosphorus nanosheets via edge-selective bonding of sacrificial C_{60} molecules. Nat Commun 2018;9(1):4177.
[72] Zhang Z, He D, Liu H, Ren M, Zhang Y, Qu J, et al. Synthesis of graphene/black phosphorus hybrid with highly stable P–C bond towards the enhancement of photocatalytic activity. Environ Pollut 2019;245:950–6.
[73] Wang X, Xiang Y, Zhou B, Zhang Y, Wu J, Hu R, et al. Enhanced photocatalytic performance of Ag/TiO_2 nanohybrid sensitized by black phosphorus nanosheets in visible and near-infrared light. J Colloid Interface Sci 2019;534:1–11.
[74] Wang X, Zhou B, Zhang Y, Liu L, Song J, Hu R, et al. *In-situ* reduction and deposition of Ag nanoparticles on black phosphorus nanosheets co-loaded with graphene oxide as a broad spectrum photocatalyst for enhanced photocatalytic performance. J Alloys Compd 2018;769:316–24.
[75] Hu J, Ji Y, Mo Z, Li N, Xu Q, Li Y, et al. Engineering black phosphorus to porous g-C_3N_4–metal–organic framework membrane: a platform for highly boosting photocatalytic performance. J Mater Chem A 2019;7(9):4408–14.
[76] Han C, Li J, Ma Z, Xie H, Waterhouse GIN, Ye L, et al. Black phosphorus quantum dot/g-C_3N_4 composites for enhanced CO_2 photoreduction to CO. Sci Chin Mater 2018;61(9):1159–66.
[77] Hu J, Guo Z, McWilliams PE, Darges JE, Druffel DL, Moran AM, et al. Band gap engineering in a 2D material for solar-to-chemical energy conversion. Nano Lett 2016;16(1):74–9.
[78] Bai L, Wang X, Tang S, Kang Y, Wang J, Yu Y, et al. Black phosphorus/platinum heterostructure: a highly efficient photocatalyst for solar-driven chemical reactions. Adv Mater 2018;30(40):1803641.
[79] Zhou Q, Chen Q, Tong Y, Wang J. Light-induced ambient degradation of few-layer black phosphorus: mechanism and protection. Angew Chem Int Ed Engl 2016;55(38):11437–41.
[80] Tang X, Liang W, Zhao J, Li Z, Qiu M, Fan T, et al. Fluorinated phosphorene: electrochemical synthesis, atomistic fluorination, and enhanced stability. Small 2017;13(47):201702739.
[81] Liu Y, Liu Z, Huang D, Cheng M, Zeng G, Lai C, et al. Metal or metal-containing nanoparticle@MOF nanocomposites as a promising type of photocatalyst. Coord Chem Rev 2019;388:63–78.